ROYAL SOCIETY OF CHEMISTRY

EDGE ARTICLE

Check for updates

All publication charges for this article have been paid for by the Royal Society of Chemistry

Unveiling hydrogen-source-dominated CO_2 electroreduction activity on nitrogen-doped carbon nanotubes

Yifan Jiang,[a] Jingyu Wang,[a] Jiaqi Xiang,[a] Haichuan He,[b] Liren Xiong,[a] Min Zhang,[c] Mustapha Abdulhadi,[a] Liu Deng, ✶[a] Shanyong Chen ✶[a] and You-Nian Liu ✶[ad]

In general, the activation of CO_2—rather than the availability of hydrogen source—is considered to be the determining step in electrocatalytic CO_2 reduction reaction (eCO_2RR) processes. However, the dissociation of H_2O, which is the dominant hydrogen source in most metal-based catalysts for the eCO_2RR in alkaline/neutral and even acidic electrolytes, suffers from the challenges of high dissociation barrier and carbonate formation. Herein, we design nitrogen-doped carbon nanotubes (N-CNTs). N-CNTs possess weak H_2O dissociation ability and can switch the hydrogen source from the dissociation of H_2O to hydrated protons, thereby greatly enhancing the eCO_2RR activity. *In situ* characterization and theoretical calculations confirm that the protons, rather than H_2O, act as the hydrogen source on the N-CNTs catalyst in an acidic electrolyte, which boosts the proton-coupled electron transfer process of *COOH formation and lowers the eCO_2RR barrier. Impressively, N-CNTs exhibit a remarkable faradaic efficiency of CO (FE_{CO}) at current densities ranging from −50 to −350 mA cm^{-2} and sustained FE_{CO} at 200 mA cm^{-2}, outperforming most reported carbon catalysts. These findings identify the hydrogen source pathway as a new activity-tuning parameter for the eCO_2RR, paving a new path for the design of efficient electrocatalytic systems.

Introduction

The electrochemical CO_2 reduction reaction (eCO_2RR) represents a promising approach to converting CO_2 into high-value-added chemicals under mild conditions.[1–3] The eCO_2RR process involves multiple proton and electron transfer processes for multiple product formation.[4,5] For instance, a typical 2e$^-$ pathway for the eCO_2RR to produce CO includes three steps: (i) a CO_2 molecule is activated after a one-electron transfer (ET, eqn (1)) step to form the intermediate *CO_2^- (* indicates the catalytic site); (ii) CO_2^- is protonated to form the active intermediate *COOH (eqn (2)), and (iii) *COOH is further protonated to form CO (eqn (3)).[6–8] Additionally, a proton-coupled electron transfer (PCET) pathway to directly activate a CO_2 molecule to *COOH *via* the integration of eqn (1) and (2) has also been proposed.[9,10] According to recent studies, the conversion of CO_2

to *COOH through proton-coupling is generally considered the rate-limiting step (RLS).[10–12]

$$* + CO_2\,(g) + e^- \rightarrow *CO_2^- \tag{1}$$

$$*CO_2^- + H^+\,(aq.) \rightarrow *COOH \tag{2}$$

$$*COOH + H^+\,(aq.) + e^- \rightarrow * + CO\,(g) + H_2O\,(l) \tag{3}$$

Considering the stability of the C=O bonds in the CO_2 molecule, great efforts have been devoted to activating CO_2 for enhancing the eCO_2RR, including catalyst design,[13] microenvironment regulation,[14] and electrolyte engineering.[15] Tuning the electronic structure of the catalytic metal centers has been regarded as the prevalent strategy to promote CO_2 activation.[16,17] In contrast, the hydrogen source process, which is one of the essential processes in PCET, has received limited attention. Generally, in alkaline, neutral, and even acidic electrolytes, the dissociation of H_2O provides the hydrogen source for the subsequent PCET step.[18] Considering the high barrier of H_2O dissociation, research has focused on exploiting effective strategies to promote H_2O dissociation. For instance, Hou *et al.* designed a catalyst in which atomically dispersed Ni sites were coupled with Ni nanoparticles (Ni@NiNCM), in which the Ni nanoparticles facilitated H_2O activation toward enhanced PCET.[19] Our group reported systems in which NiPc was loaded

aHunan Provincial Key Laboratory of Micro & Nano Materials Interface Science, College of Chemistry and Chemical Engineering, Central South University, Changsha, Hunan 410083, PR China. E-mail: dengliu@csu.edu.cn; shanyongchen@csu.edu.cn; liuyounian@csu.edu.cn

bSchool of Chemistry and Chemical Engineering, University of South China, Hengyang, Hunan 421001, PR China

cCollege of Materials and Energy, Foshan University, Foshan, Guangdong 528000, PR China

dCollege of Materials, Chemistry and Chemical Engineering, Hangzhou Normal University, Hangzhou, Zhejiang 311321, PR China
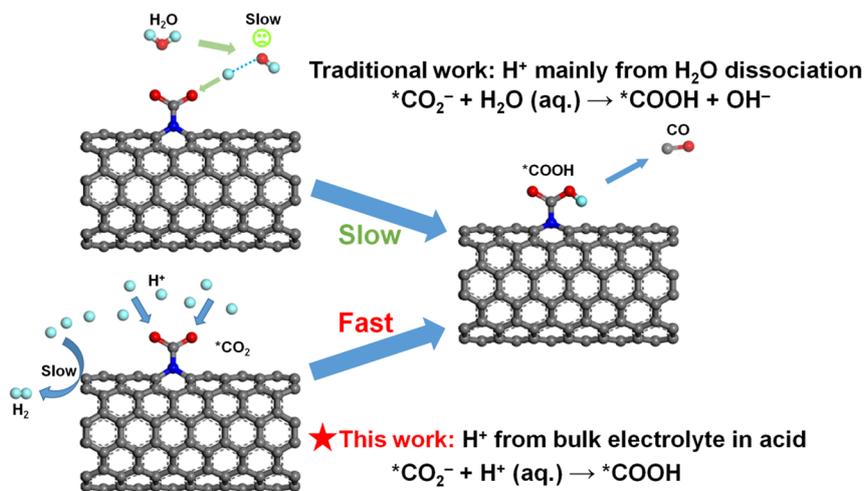
Fig. 1 Schematic of the eCO$_2$RR on traditional catalytic systems and the present system using N–CNTs in an acidic system.

on sulphur (S)-doped CNTs, in which the S atoms enabled the facilitation of the H$_2$O dissociation and thus the PCET processes.[20] However, in systems in which H$_2$O acts as the proton donor, excessive hydroxide ion (OH$^-$) accumulation occurs at the catalytic interface, which drives the irreversible precipitation of carbonate/bicarbonate species (CO$_3^{2-}$/ HCO$_3^-$).[21] This ultimately impairs both the CO$_2$ conversion efficiency and long-term device durability, with particularly pronounced degradation at high-current-density operation.[22,23] Notably, the use of protons as the hydrogen source offers a potential solution to these issues, but challenges remain.[24–26] The traditional active metal sites show both strong activity for H$_2$O dissociation and proton reduction in an acidic electrolyte, and prioritize the hydrogen source pathway from H$_2$O dissociation even in strongly acidic electrolytes.[27–29] Metal-free carbon-based materials exhibit relatively weak H$_2$O dissociation activity,[30] making them an attractive platform for the employment of protons as a hydrogen source for the eCO$_2$RR in acidic electrolyte. Furthermore, the effect of the hydrogen source on the eCO$_2$RR remains unexplored.

Herein, we have designed a catalyst based on nitrogen-doped carbon nanotubes (N-CNTs) and employed it to investigate the effect of the hydrogen source on the eCO$_2$RR pathway. Our study reveals that the protons in acidic electrolyte function as the proton source, which differs fundamentally from the general metal-based catalysts that use H$_2$O dissociation as the proton source. Switching the hydrogen source from H$_2$O dissociation to hydrated protons bypasses the high barrier of H$_2$O dissociation, thereby accelerating the PCET process and eCO$_2$RR kinetics (Fig. 1). Importantly, a counterintuitive but prominent improvement in eCO$_2$RR performance is observed in acidic electrolyte compared to neutral electrolyte. The N-CNTs achieve a FE$_{CO}$ of 85% at a high current density of 350 mA cm^{-2} in a flow cell, outperforming most reported carbon materials. *In situ* spectroscopy and kinetic experiments reveal that in acidic electrolyte, H$^+$ can act directly as the proton donor to promote CO$_2$ protonation to form *COOH. Theoretical analysis also confirms the lowered reaction barrier of *COOH formation.

This work highlights the crucial effect of proton-coupled electron transfer on improving eCO$_2$RR performance in acidic electrolytes, providing new insights for the design of high-performance eCO$_2$RR systems and beyond.

Results and discussion

Preparation and characterization of the catalyst

N-CNTs were prepared through a pyrolysis strategy, in which dicyandiamide (DCD) was selected as the nitrogen (N) source (Fig. 2a, for details, see the Experimental section in the SI). The structural characterizations were performed by X-ray diffraction (XRD). As displayed in Fig. 2b, the diffraction peaks of the N-CNTs and CNTs were assigned to the graphite, indicating the absence of metal species. The (003) peak indicates the graphitic nature and high crystallinity maintained by the N-CNTs. Morphological characterizations of the N-CNTs were conducted using scanning electron microscopy (SEM) and transmission electron microscopy (TEM). As displayed in Fig. 2c, the N-CNTs maintain the tubular feature and the mean tube diameter is around 35 nm, indicating no significant changes in the carbon nanotube morphology after N-doping. TEM images indicate that the N-CNTs show a multiwalled morphology with a lattice fringe distance of 0.33 nm at the edge, corresponding to the (003) plane of graphitized carbon (Fig. 2d). The elemental mapping images present a homogeneous distribution of N in single N-CNTs. The Raman spectrum (Fig. 2e) shows a strong G-band at 1570 cm^{-1} and D-band at 1345 cm^{-1}. The intensity ratio of the D peak to the G peak (I_D/I_G) for the N-CNTs is 0.79, which is higher than that of CNTs ($I_D/I_G = 0.68$). The N-doping in the carbon nanotubes results in local defects on the carbon atom layer, which is responsible for the increase in the I_D/I_G ratio of the N-CNTs. To analyze the atomic electron state and coordination environment, X-ray photoelectron spectroscopy (XPS) and X-ray absorption energy near edge-structure (XANES) spectroscopy were carried out. The XPS survey spectrum further confirms the presence of N with a content of 1.62% (Fig. S1 and Table S1). As shown in Fig. 2f, the three peaks at 398.9, 399.8
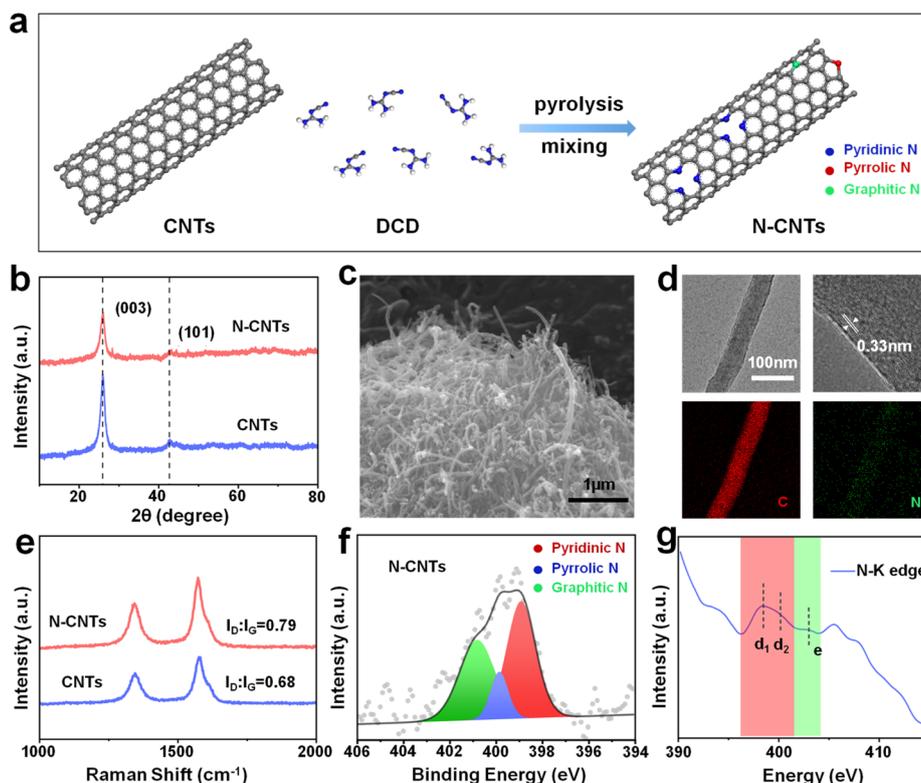
Fig. 2 (a) Illustration of the preparation of N-CNTs. The blue, red and green spheres represent pyridinic N, pyrrolic N and graphitic atoms. (b) XRD patterns of CNTs and N-CNTs. (c) SEM and (d) TEM and element mapping images of N-CNTs. (e) Raman spectra of CNTs and N-CNTs. (f) N 1s XPS spectrum for N-CNTs. (g) N K-edge XANES spectrum for N-CNTs.

and 401 eV correspond to pyridinic, pyrrolic, and graphitic N species in the sp^2 carbon network, respectively.[31,32] For the N K-edge XANES spectra (Fig. 2g), the d_1, d_2, and e peaks are assigned to pyridinic N, pyrrolic N, and graphitic N, respectively.[33–35]

Hydrogen-source-dominated eCO₂RR performance

Next, the eCO₂RR performances at different pH values regulated by H_2SO_4 were evaluated. An anion exchange membrane (Nafion-117) was used to separate the cathode and anode in a three-electrode H-cell reactor. Carbon paper loaded with the N-CNTs was used as the working electrode. The electrochemical tests were performed in H_2SO_4 electrolyte containing 0.6 M K_2SO_4 (pH = 2). The gaseous and liquid products from the eCO₂RR were measured using on-line gas chromatography and ¹H nuclear magnetic resonance (¹H NMR). The linear sweep voltammetry (LSV) curve of the N-CNTs exhibits a more-positive onset potential and larger negative currents in the CO₂-purged electrolyte than in the N₂-purged one (Fig. S2). Conversely, the onset potential of the CNTs in a CO₂ atmosphere is more negative compared to that in N₂-purged conditions, indicating the minimal eCO₂RR activity on the CNTs. The negative onset potential may be induced by the suppressed HER due to the generation of potassium carbonate and bicarbonate (Fig. S3) at the electrolyte surface after the introduction of CO₂.[21] Consequently, the eCO₂RR products were investigated under potentiostatic electrolysis. The current–time (i–t) curves and FE_CO are

shown in Fig. S4a and b. The N-CNTs exhibit an excellent FE_CO above 80% in the range from −1.2 to −1.4 V vs. SHE, which is much higher than that of the CNTs (Fig. S5), indicating their superior activity in the eCO₂RR. ¹H NMR results exclude the presence of liquid products during the eCO₂RR (Fig. S6). Next, the eCO₂RR performances of the N-CNTs at different pH values were evaluated to explore the effect of proton concentration on the kinetics of the catalytic reaction. Three 0.6 M K_2SO_4 solutions with different pH values (pH = 2, 4, and 7) were selected for eCO₂RR testing. The linear sweep voltammetry (LSV) curves acquired in CO₂-saturated electrolyte show that the onset potential is −0.7 V vs. SHE at pH = 2, which is 0.4 V lower than that at pH = 7 (Fig. S2). In sharp contrast, there is no obvious change in the onset potential as the pH changes in N₂-saturated electrolyte. Importantly, the partial current densities of CO (j_{CO}) at the onset potential ranges were calculated for the three electrolytes (pH = 2, pH = 4, pH = 7). As shown in Fig. 3a and Tables S2–S4, the onset potential for eCO₂RR shows a significant positive shift in a strongly acidic electrolyte (pH = 2) compared to a neutral electrolyte (pH = 7), which implies the promoting effect of protons on the eCO₂RR. Additionally, there is no significant change in the LSV curves acquired in N₂-saturated electrolytes as the pH is changed, indicating that the proton concentration has no significant effect on the activity of the HER in this system. Three representative potentials, i.e., −1.3, −1.4 and −1.5 V vs. SHE, were then selected to perform constant-potential electrolysis. As shown in Fig. S8, the typical
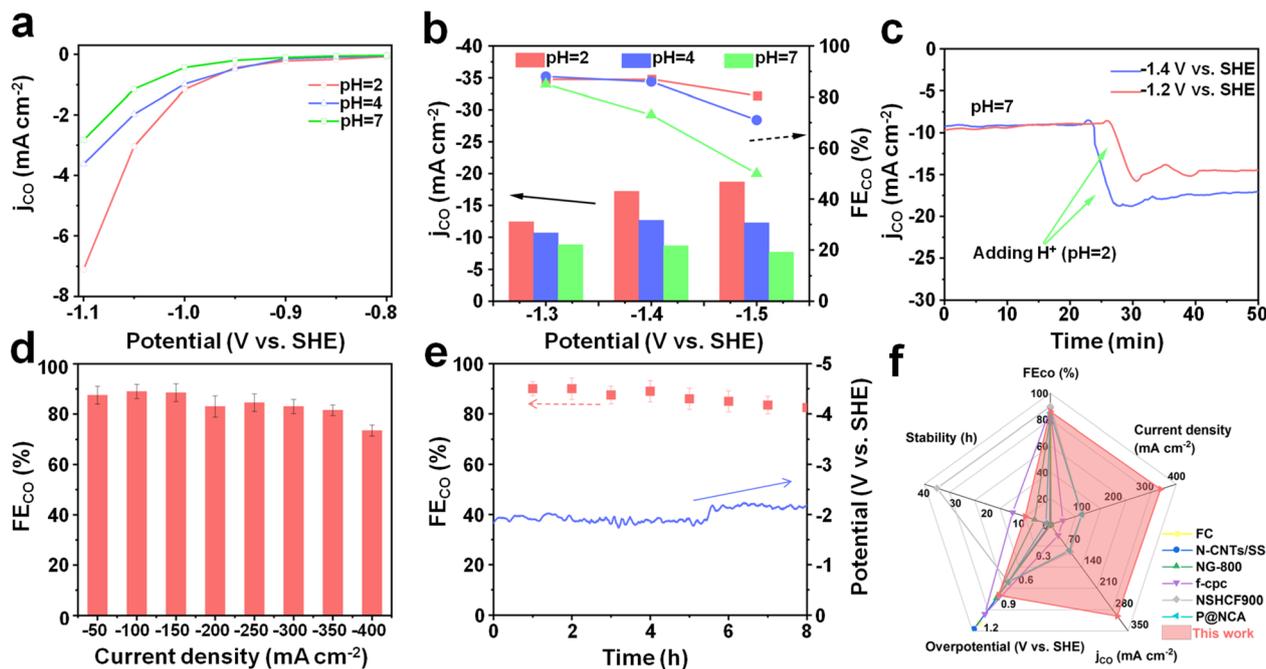
Fig. 3 (a) Values of j_{CO} at various applied potentials for the onset range. (b) FE_{CO} and j_{CO} values of the N-CNTs in electrolytes with different pH. (c) j_{CO} curves (i–t) of the N-CNTs with the addition of H_2SO_4. (d) FE_{CO} of the N-CNTs at different current densities in a flow cell. (e) eCO$_2$RR stability of the N-CNTs at 200 mA cm^{-2} in a flow cell. (f) Comparison of the eCO$_2$RR activity of the N-CNTs with those of other reported metal-free carbon catalysts.

metal-based catalysts Au and nickel phthalocyanine (NiPc) show much lower FE_{CO} at pH = 2 than at pH = 7 due to the prior occurrence of the HER on the metal sites. In contrast, the reduction in pH not only does not compromise catalytic selectivity, but also enhances catalytic activity for the N-CNTs (Fig. 3b and S7). At a cathode potential of −1.3 V *vs.* SHE, the FE_{CO} can be maintained at 85% at all three pH values. When the cathode potential is −1.4 V *vs.* SHE, the FE_{CO} values in acidic electrolyte (pH = 2 and pH = 4) are comparable, but superior to that in neutral electrolyte at pH = 7 (77%). When the cathode potential is −1.5 V *vs.* SHE, the FE_{CO} in neutral electrolyte decreases to 50%, while the FE_{CO} in acidic electrolyte decreases only slightly. This may originate from insufficient timely replenishment of protons and the active sites being occupied by H_2O molecules for the HER. The rate of the eCO$_2$RR to produce CO can be evaluated by measuring the j_{CO}. As shown in Fig. 3b, at cathode potentials of −1.3, −1.4 and −1.5 V *vs.* SHE, the j_{CO} increases with decreasing pH, with the j_{CO} at pH = 2 being the highest among these systems. Importantly, the j_{CO} increases from 7.6 mA cm^{-2} at pH = 7 to 18.7 mA cm^{-2} at pH = 2, indicating that the hydrogen source dominated the eCO$_2$RR performance. The same trend can also be observed in Fig. 3c and S9. The j_{CO} increases sharply with the addition of acid, indicating that the protons can efficiently promote the eCO$_2$RR activity on the N-CNTs. It also can be inferred that, in the eCO$_2$RR, the protons originate from the acidic protons rather than from H_2O molecules.

N-CNTs demonstrate promising performance in acidic electrolyte. To further increase the catalytic current density and production rate for industrial applications, we explored their

eCO$_2$RR performance in a flow cell reactor. In the flow cell, the utilization of gas diffusion electrodes minimized mass transport limitations and significantly enhanced the rate of the eCO$_2$RR. The eCO$_2$RR products were investigated under constant-current electrolysis. Impressively, the N-CNTs in the acidic flow cell showed an FE_{CO} of over 80% at current densities up to 350 mA cm^{-2} (Fig. 3d and S10, S11). Moreover, the eCO$_2$RR stability of the N-CNTs at an industrial-level current density of 200 mA cm^{-2} was tested. As shown in Fig. 3e, the FE_{CO} remained over 80% during 8 h of continuous reaction, suggesting excellent durability. This catalytic system presents remarkable eCO$_2$RR performance in terms of various performance parameters compared with reported metal-free eCO$_2$RR catalysts (Fig. 3f and Table S5), verifying the substantial advantages of using N-CNTs in acidic electrolyte. Impressively, the carbon-based N-CNTs catalyst shows comparable eCO$_2$RR performance to the reported metal-based systems in acidic media (Table S6), demonstrating the effectiveness of using protons as the hydrogen source to enhance the eCO$_2$RR.

Effect of different hydrogen sources on the eCO$_2$RR

Next, we focused on the origin of the enhanced eCO$_2$RR performance in acidic electrolyte. First, the intrinsic electrochemical kinetics and the rate-limiting step (RLS) of the N-CNTs were examined using Tafel slope analysis in the kinetic-controlled regime. The Tafel slopes (Fig. S12) at pH = 2, 4 and 7 were determined to be 171, 171 and 177 mV dec^{-1}, respectively, which are close to the theoretical value of the CO_2 protonation step as the RLS.[8,36–38] Additionally, to investigate the intrinsic electrochemical kinetics of the CO_2 protonation step,

we carried out Tafel slope analysis under different CO_2 partial pressures (p_{CO_2}) and compared the three sets of results, as shown in Fig. S13. The Tafel slopes are 171, 171 and 281 mV dec^{-1} under the three conditions of 100%, 50% and 20% p_{CO_2}, respectively. The Tafel slope is observed to gradually increase with decreasing p_{CO_2}, indicating that p_{CO_2} can also influence the eCO$_2$RR rate. The rate-limiting step (RLS) in this process is identified as PCET.[39] To investigate the proton transport behavior, we employed the rotating disk electrode (RDE) technique in two different electrolytes (CO_2-saturated 0.6 M K_2SO_4 electrolyte with the pH adjusted to 2 or 7 using H_2SO_4). As shown in Fig. 4a and S14, at a given rotation rate, the current at pH = 2 is significantly larger than that at pH = 7, which is consistent with the LSV and i–t results. Furthermore, the current shows a much more pronounced dependence on the rotation rate in the pH = 2 electrolyte. At potentials of −1.2, −1.3, −1.4 V vs. SHE, the FE$_{CO}$ values in the eCO$_2$RR test all exceed 80%. In the pH = 2 electrolyte, the current shows a distinct linear relationship with rotation speed, and the slopes were calculated to be 0.256, 0.252, 0.273 at −1.2, −1.3, −1.4 V vs. SHE, respectively. However, in the pH = 7 electrolyte, this relationship was weak, with slopes near zero (0.002, 0.009, 0.022). The enhanced slopes at pH = 2 provide evidence that the

protons can be directly transferred to the catalyst surface to participate in the eCO$_2$RR.[40] The kinetic isotope effect (KIE) was measured to further evaluate the effect of the proton source on the reaction kinetics. We designed two KIE experiments under neutral (pH = 7) and acidic (pH = 2) (Fig. S15 and S16) electrolyte, respectively. As shown in Fig. 4b, the KIE values at pH = 7 were determined to be 1.60, 1.58, and 1.61 at −1.2, −1.3 and −1.4 V vs. SHE, which implies that the sluggish proton supply, likely resulting from the processes of water dissociation, limits the eCO$_2$RR kinetics. The KIE values decreased to 1.19, 1.21, and 1.19 at −1.2, −1.3, −1.4 V vs. SHE in acid, suggesting that the free protons can facilitate the eCO$_2$RR kinetics. Having demonstrated the accelerated proton-coupled process kinetics in acidic electrolyte, we subsequently investigated the coverage of adsorbed hydrogen (*H) over the N-CNTs surface via in situ EIS measurements. The double-parallel equivalent circuit model was used to simulate the Nyquist plots (Fig. 4c, S17 and Tables S7, S8). The *H coverage can be depicted by the adsorption pseudo-capacitance (C_φ) referring to the *H adsorption charge.[4,41,42] The N-CNTs exhibited higher *H coverage in the acidic condition (pH = 2) than the neutral one (pH = 7), as evidenced by the increased C_φ at every potential (Fig. 4d).
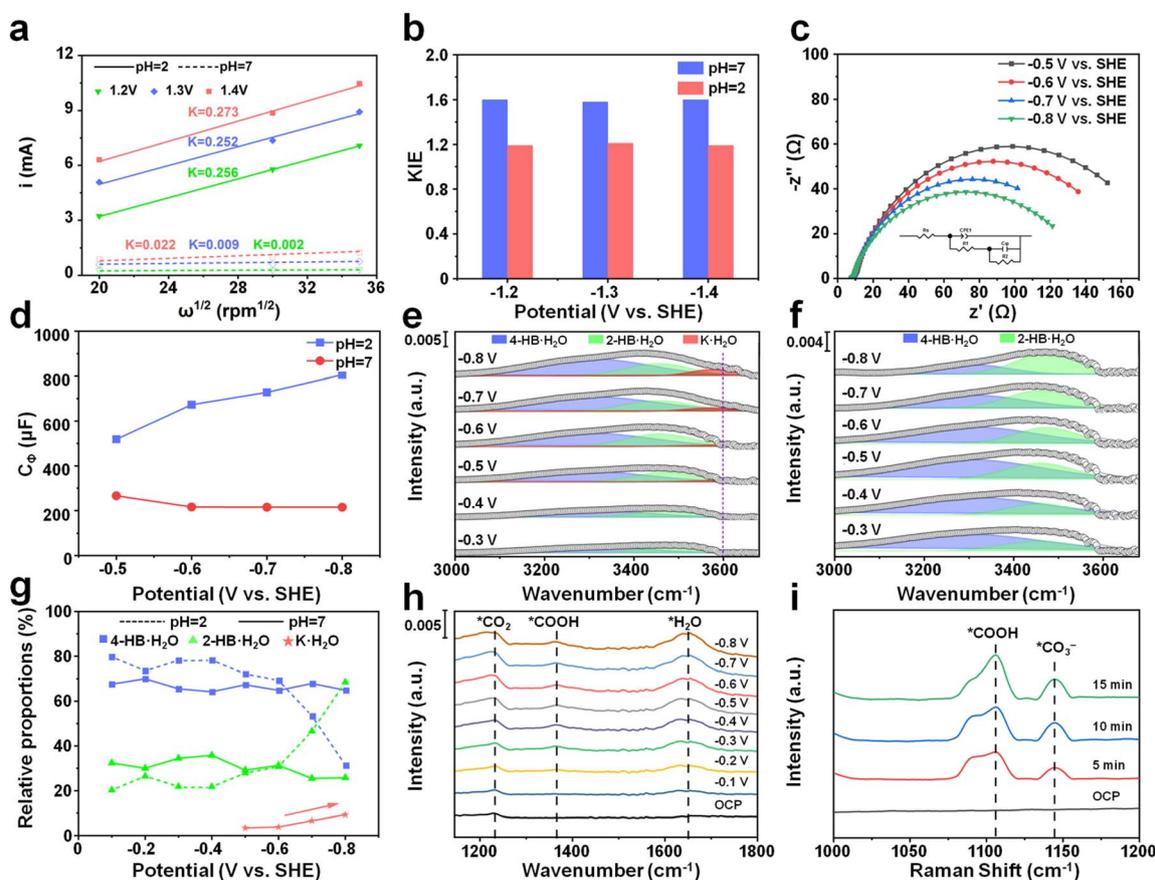

Fig. 4 (a) Linear fitting of i vs. $\omega^{1/2}$ on the RDE. (b) KIE values of H/D at pH = 7 and H$^+$/D$^+$ at pH = 2. (c) EIS data and fitting results for the N-CNTs at pH = 2. (d) Calculated C_φ values of the N-CNTs at different pH values. In situ ATR-SEIRAS measurements for Gaussian fitting of the O−H stretching modes of the N-CNTs (e) at pH = 7 and (f) pH = 2. (g) Potential-dependent relative proportion of interfacial water for the N-CNTs at pH = 2 and pH = 7. (h) In situ ATR-SEIRAS spectra for reaction intermediates. (i) In situ Raman spectra for reaction intermediates.

The *in situ* attenuated total reflection Fourier transform infrared spectroscopy (ATR-FTIR) results show the O–H stretching band ranging from 3000 to 3800 cm^{-1}, which was deconvoluted into three Gaussian peaks, namely, 4-coordinated hydrogen-bonded water (4-HB·H_2O, blue), 2-coordinated hydrogen-bonded water (2-HB·H_2O, green), and K^+-hydrated water (K·H_2O, red).[13] Notably, K·H_2O serves as the dominant proton donor for the eCO$_2$RR protonation steps. The K·H_2O exhibits a more ordered solvation structure and proximity to the electrode interface, which enables efficient transport of H_2O molecules to the catalytically active sites, facilitating continuous proton supply from H_2O.[13] As shown in Fig. 4e, in a neutral electrolyte, an increase in K·H_2O at the electrode surface is observed with increasing cathodic bias, consistent with electric-field-enhanced cation hydration. Conversely, in an acidic electrolyte, proton-dominated interfacial chemistry completely suppresses K^+ hydration, as confirmed by the absence of the characteristic O–H stretching modes of K·H_2O (Fig. 4f), confirming that K·H_2O cannot function as the proton source in an acidic electrolyte with the N-CNTs catalyst. Furthermore, in neutral electrolyte, the intensity of the high-frequency 2-HB·H_2O peak progressively decreases with increasing cathodic potential, as shown by the dotted curves in Fig. 4g. In contrast, acidic electrolyte produces opposite spectral responses: the same 2-HB·H_2O peak intensifies, while the low-frequency 4-HB·H_2O peak attenuates with applied cathodic polarization (solid curves in Fig. 4g). These results suggest that H_2O molecules exhibit stronger binding affinity to N-CNT surfaces in neutral electrolytes, thereby serving as more effective proton donors for the eCO$_2$RR. In contrast, the interaction weakens significantly in acidic environments, likely due to the competitive proton adsorption disrupting the hydrogen-bonding networks at the H_2O/N-CNT interface, thereby reducing interfacial water stability.[43,44] Here, the high surface concentration of hydrated protons enables direct proton transfer to CO$_2$ reduction intermediates, bypassing the cation-mediated hydration pathway observed in neutral electrolytes. The enrichment of *H on the N-CNTs surface supported by the acidic electrolyte can facilitate the proton-coupled CO$_2$ to *COOH process. In contrast, in a neutral electrolyte, interfacial H_2O molecules near the catalytically active sites act as proton donors for the protonation step, which features slower kinetics compared to acidic electrolytes.

In addition, distinct vibrational bands corresponding to the *CO$_2$ intermediate and *COOH adsorbate are observed at 1220 cm^{-1} and 1363 cm^{-1}, respectively. Concurrently, the characteristic peak at 1660 cm^{-1} arises from the symmetric bending mode (δ-H_2O) of interfacial H_2O (Fig. 4h).[45–48] With the acceleration of the eCO$_2$RR at the more negative potentials, the peak at 1363 cm^{-1} is gradually reinforced, indicating that the *COOH intermediate is continuously generated.[49–51] *In situ* Raman testing was carried out simultaneously with the constant-potential electrolysis (−0.3 V *vs.* SHE). The two obvious peaks located at 1106 and 1145 cm^{-1} were assigned to *COOH and *CO$_3^-$, further proving the generation of adsorbed *COOH intermediate (Fig. 4i).[6,49,52] The CO$_2$ temperature-programmed desorption (CO$_2$-TPD) curves of the N-CNTs revealed the

enhanced CO$_2$ activation on N-CNTs, which may result from the doped alkaline N atoms in the carbon matrix (Fig. S18).

Mechanism of the eCO$_2$RR

To probe the catalytically active sites, four kinds of N-CNTs were prepared using ratios of nitrogen source to CNT of 1 : 6, 1 : 3, 1 : 2, and 1 : 1; these are denoted as N-CNTs$_6$, N-CNTs$_3$, N-CNTs$_2$, and N-CNTs, respectively. The XRD, Raman and SEM results shown in Fig. S19, S20 and S21 indicate the successful preparation of the four kinds of N-CNTs. Through analysis of the XPS survey spectra (Fig. S22), the total nitrogen contents were determined to be 1.58%, 1.60%, 1.69%, and 1.62% for the N-CNTs$_6$, N-CNTs$_3$, N-CNTs$_2$, and N-CNTs, respectively. The four types of N-CNTs contain pyridinic N, pyrrolic N, and graphitic N (Fig. S23). We tested their FE$_{CO}$ at constant potentials of −1.2, −1.3 and −1.4 V *vs.* SHE (Fig. S24) and selected the average FE$_{CO}$ of these three potentials to differentiate the activity contributions from different nitrogen species. As illustrated in Fig. 5a, the average FE$_{CO}$ has a positive correlation with the pyridinic nitrogen content. As the pyridinic N atom content increases from 12.6% to 50.5%, the average FE$_{CO}$ increases from 49% to 85%. The N K-edge XANES spectra for N-CNTs$_6$ and N-CNTs are shown in Fig. 5b. Compared with that of N-CNTs$_6$, the peak intensity of pyridinic N in the N-CNTs is higher, while the peak intensity of pyrrolic N in N-CNTs$_6$ is higher. This indicates that the N-CNTs have a greater content of pyridinic N, whereas the N-CNTs$_6$ have a greater content of pyrrolic N, consistent with the XPS results. This indicates that the pyridinic N species in the N-CNTs mainly contribute to eCO$_2$RR activity. DFT calculations were performed to theoretically investigate the effect of electrolyte pH on the catalytic system and to elucidate the mechanism of CO production *via* eCO$_2$RR over the N-CNTs catalyst (Fig. 5c, d and S25, S26). Based on the experimental and characterization results, the pyridinic N was selected as the eCO$_2$RR active site. The optimized adsorption models of the different
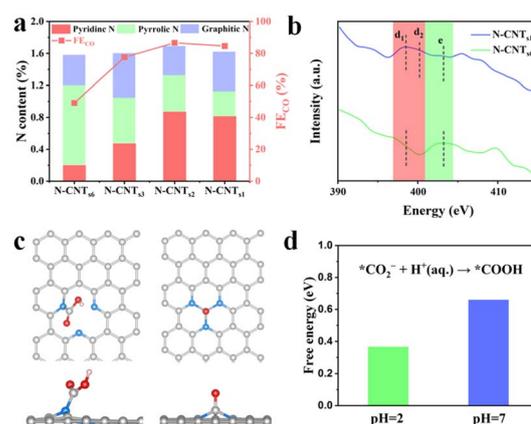

Fig. 5 (a) FE$_{CO}$ and the contents of three kinds of N species for N-CNTs$_6$, N-CNTs$_3$, N-CNTs$_2$ and N-CNTs. (b) N K-edge XANES spectra for N-CNTs$_6$ and N-CNTs. (c) Reaction configurations on the N-CNTs based on the *COOH and *CO adsorption intermediates after optimization. The blue, red and gray spheres represent N, O and C atoms. (d) Gibbs free energy diagrams of the conversion of CO$_2$ to CO over the N-CNTs with the free energy correction for pH = 2 and 7.

intermediates in the CO_2 to CO process are shown in Fig. 5c. Notably, the most endothermic reaction step in both acidic and neutral electrolytes is the protonation of CO_2 to form the *COOH intermediate, which serves as the RLS. The energy barrier (ΔG) value for the protonation of CO_2 is 0.365 eV on pyridinic N-doped carbon at pH = 2, which is lower than that at pH = 7 (0.66 eV), indicating that acidic conditions are more favorable for the eCO_2RR on N-CNTs. Additionally, the ΔG on graphitic N was also calculated (see Fig. S26). Compared to pyridinic N, the much higher ΔG values on graphitic N exclude the graphitic N sites as active centers and demonstrate that the eCO_2RR performance originates from pyridinic N. These DFT results parallel the experimental findings, jointly confirming that acid electrolyte accelerates the proton-coupled electron transfer for *COOH formation on the N-CNTs and thus enhances eCO_2RR performance.

Conclusion

In summary, we developed a new strategy to enhance the eCO_2RR performance on the metal-free N-CNTs catalyst by directly utilizing protons from the acidic electrolyte to accelerate the proton-coupled electron transfer process. The N-CNTs were prepared *via* a facile pyrolysis route and verified using XPS and XANES. When using the N-CNTs as an eCO_2RR catalyst, the acidic environment provides sufficient protons to couple with CO_2 and enhances the eCO_2RR performance. Impressively, remarkable eCO_2RR performances were achieved with the N-CNTs in acidic electrolyte, with an FE_{CO} of above 80% from 50 to 350 mA cm^{-2}, exceeding those of most reported metal-free catalysts. The hydrated protons can be used as a proton source in an acidic electrolyte, which promotes the proton-coupled electron transfer process as evidenced by *in situ* experimental investigations under different pH conditions. Furthermore, the promoted process of *COOH formation is identified by *in situ* ATR-FTIR and *in situ* Raman analysis, which lowers the reaction barrier of RDS, as confirmed by DFT calculations. This work highlights the important effect of proton supply on eCO_2RR performance, affording new insights for the development of an electrocatalysis system.

Author contributions

Yifan Jiang: experiment design, data analysis, conceptualization and original draft and writing. Jingyu Wang, Jiaqi Xiang, and Liren Xiong: preparation of sample, date curation and investigation. Haichuan He: sample characterization, data analysis. Min Zhang and Mustapha Abdulhadi: theoretical calculation and analysis. Liu Deng: reviewing manuscript. Shanyong Chen and You-Nian Liu: supervision, funding acquisition, project visualization, and reviewing manuscript.

Conflicts of interest

The authors declare no conflict of interest.

Data availability

The data supporting this article have been included as part of the supplementary information (SI). Supplementary information is available. See DOI: https://doi.org/10.1039/d5sc08737f.

Acknowledgements

Notes and references

1 W. Li, Z. Yin, Z. Gao, G. Wang, Z. Li, F. Wei, X. Wei, H. Peng, X. Hu, L. Xiao, J. Lu and L. Zhuang, *Nat. Energy*, 2022, **7**, 835–843.

2 R. I. Masel, Z. Liu, H. Yang, J. J. Kaczur, D. Carrillo, S. Ren, D. Salvatore and C. P. Berlinguette, *Nat. Nanotechnol.*, 2021, **16**, 118–128.

3 S. P and S. K. Mandal, *Chem. Sci.*, 2020, **11**, 10571–10593.

4 S. Chen, X. Li, C. W. Kao, T. Luo, K. Chen, J. Fu, C. Ma, H. Li, M. Li, T. S. Chan and M. Liu, *Angew. Chem., Int. Ed.*, 2022, **61**, e202206233.

5 W. Ge, Y. Chen, Y. Fan, Y. Zhu, H. Liu, L. Song, Z. Liu, C. Lian, H. Jiang and C. Li, *J. Am. Chem. Soc.*, 2022, **144**, 6613–6622.

6 H. Zhang, C. Xu, X. Zhan, Y. Yu, K. Zhang, Q. Luo, S. Gao, J. Yang and Y. Xie, *Nat. Commun.*, 2022, **13**, 6029.

7 H. Zhang, J. Gao, D. Raciti and A. S. Hall, *Nat. Catal.*, 2023, **6**, 807–817.

8 W. Deng, P. Zhang, B. Seger and J. Gong, *Nat. Commun.*, 2022, **13**, 803.

9 X. Duan, J. Xu, Z. Wei, J. Ma, S. Guo, S. Wang, H. Liu and S. Dou, *Adv. Mater.*, 2017, **29**, 1701784.

10 H. Yang, Y. Wu, Q. Lin, L. Fan, X. Chai, Q. Zhang, J. Liu, C. He and Z. Lin, *Angew. Chem., Int. Ed.*, 2018, **57**, 15476–15480.

11 S. Vijay, W. Ju, S. Brückner, S.-C. Tsang, P. Strasser and K. Chan, *Nat. Catal.*, 2021, **4**, 1024–1031.

12 J. Rosen, G. S. Hutchings, Q. Lu, S. Rivera, Y. Zhou, D. G. Vlachos and F. Jiao, *ACS Catal.*, 2015, **5**, 4293–4299.

13 Q. Zhang, H. J. Tsai, F. Li, Z. Wei, Q. He, J. Ding, Y. Liu, Z. Y. Lin, X. Yang, Z. Chen, F. Hu, X. Yang, Q. Tang, H. B. Yang, S. F. Hung and Y. Zhai, *Angew. Chem., Int. Ed.*, 2023, **62**, e202311550.

14 J. Resasco, L. D. Chen, E. Clark, C. Tsai, C. Hahn, T. F. Jaramillo, K. Chan and A. T. Bell, *J. Am. Chem. Soc.*, 2017, **139**, 11277–11287.

15 K. Xu, J. Li, F. Liu, X. Chen, T. Zhao and F. Cheng, *Angew. Chem., Int. Ed.*, 2023, **135**, e202311968.

16 S. Wei, Y. Xu, T. Song, H. Dai, F. Li, X. Gao, Y. Zhai, S. Gong, R. Li, X. Zhang and K. Chan, *J. Am. Chem. Soc.*, 2025, **147**, 4219–4229.

17 J. Wang, Y.-C. Huang, Y. Wang, H. Deng, Y. Shi, D. Wei, M. Li, C.-L. Dong, H. Jin, S. S. Mao and S. Shen, *ACS Catal.*, 2023, **13**, 2374–2385.

18 Y. Hou, M. Qiu, M. G. Kim, P. Liu, G. Nam, T. Zhang, X. Zhuang, B. Yang, J. Cho, M. Chen, C. Yuan, L. Lei and X. Feng, *Nat. Commun.*, 2019, **10**, 1392.

19 X. Wang, X. Sang, C. L. Dong, S. Yao, L. Shuai, J. Lu, B. Yang, Z. Li, L. Lei, M. Qiu, L. Dai and Y. Hou, *Angew. Chem., Int. Ed.*, 2021, **60**, 11959–11965.

20 A. Mustapha, S. Chen, J. Xiang, Y. Jiang, J. Wang, X. Zhao, F. Chen, M. Wang, H. Zhou and K. Zeng, *Chem. Commun.*, 2024, **60**, 13243–13246.

21 X. Li, P. Zhang, L. Zhang, G. Zhang, H. Gao, Z. Pang, J. Yu, C. Pei, T. Wang and J. Gong, *Chem. Sci.*, 2023, **14**, 5602–5607.

22 W. Wu and Y. Wang, *J. Am. Chem. Soc.*, 2025, **147**, 11662–11666.

23 Z. Zhang, Q. Lu, J. Sun, G. Li, W. Wu, Z. Xu, L. Xu and Y. Wang, *Chem. Sci.*, 2024, **15**, 2786–2791.

24 X. Zou and J. Gu, *Chin. J. Catal.*, 2023, **52**, 14–31.

25 H. Qin, Y. Du, Y. Bai, F. Li, X. Yue, H. Wang, J. Peng and J. Gu, *Nat. Commun.*, 2023, **14**, 5640.

26 M. Fan, J. E. Huang, R. K. Miao, Y. Mao, P. Ou, F. Li, X. Li, Y. Cao, Z. Zhang, J. Zhang, Y. Yan, A. Ozden, W. Ni, Y. Wang, Y. Zhao, Z. Chen, B. Khatir, C. P. O'Brien, Y. Xu, Y. C. Xiao, G. I. N. Waterhouse, K. Golovin, Z. Wang, E. H. Sargent and D. Sinton, *Nat. Catal.*, 2023, **6**, 763–772.

27 Z. Jiang, S. Ren, X. Cao, Q. Fan, R. Yu, J. Yang and J. Mao, *Angew. Chem., Int. Ed.*, 2024, **63**, e202408412.

28 L. Li, Z. Liu, X. Yu and M. Zhong, *Angew. Chem., Int. Ed.*, 2023, **62**, e202300226.

29 Z. Liu, T. Yan, H. Shi, H. Pan, Y. Cheng and P. Kang, *ACS Appl. Mater. Interfaces*, 2022, **14**, 7900–7908.

30 T. Li, Y. Chen, W. Hu, W. Yuan, Q. Zhao, Y. Yao, B. Zhang, C. Qiu and C. M. Li, *Nanoscale*, 2021, **13**, 4444–4450.

31 C. Chen, X. Sun, X. Yan, Y. Wu, H. Liu, Q. Zhu, B. B. A. Bediako and B. Han, *Angew. Chem., Int. Ed.*, 2020, **59**, 11123–11129.

32 H. Liu, P. Sun, M. Feng, H. Liu, S. Yang, L. Wang and Z. Wang, *Appl. Catal., B*, 2016, **187**, 1–10.

33 J. Qin, H. Liu, P. Zou, R. Zhang, C. Wang and H. L. Xin, *J. Am. Chem. Soc.*, 2022, **144**, 2197–2207.

34 Q. Wang, M. Dai, H. Li, Y. R. Lu, T. S. Chan, C. Ma, K. Liu, J. Fu, W. Liao and S. Chen, *Adv. Mater.*, 2023, **35**, 2300695.

35 C. Ye, J. Shan, D. Chao, P. Liang, Y. Jiao, J. Hao, Q. Gu, K. Davey, H. Wang and S.-Z. Qiao, *J. Am. Chem. Soc.*, 2021, **143**, 16902–16907.

36 W. Ni, Y. Xue, X. Zang, C. Li, H. Wang, Z. Yang and Y.-M. Yan, *ACS Nano*, 2020, **14**, 2014–2023.

37 B. M. Tackett, J. H. Lee and J. G. Chen, *Acc. Chem. Res.*, 2020, **53**, 1535–1544.

38 J. Chen, Z. Li, X. Wang, X. Sang, S. Zheng, S. Liu, B. Yang, Q. Zhang, L. Lei, L. Dai and Y. Hou, *Angew. Chem., Int. Ed.*, 2021, **61**, e202111683.

39 Y. Wang, J. Kim, H. D. Jung, J. Liu, K. Ye, C. Xia, S. Back and K. Jiang, *Nano Energy*, 2024, **127**, 109728.

40 Y. Shi, Y. Yang, A. Xu, K. N. Hui, F. Li and J. Zeng, *J. Am. Chem. Soc.*, 2025, **147**, 35698–35704.

41 J. Li, H.-X. Liu, W. Gou, M. Zhang, Z. Xia, S. Zhang, C.-R. Chang, Y. Ma and Y. Qu, *Energy Environ. Sci.*, 2019, **12**, 2298–2304.

42 S. Chen, S. Wang, P. Hao, M. Li, Y. Zhang, J. Guo, W. Ding, M. Liu, J. Wang and X. Guo, *Appl. Catal., B*, 2022, **304**, 120996.

43 Z. Zhang, T. Wang, Y. Cai, X. Li, J. Ye, Y. Zhou, N. Tian, Z. Zhou and S. Sun, *Nat. Catal.*, 2024, **7**, 807–817.

44 R. Cui, Q. Yuan, C. Zhang, X. Yang, Z. Ji, Z. Shi, X. Han, Y. Wang, J. Jiao and T. Lu, *ACS Catal.*, 2022, **12**, 11294–11300.

45 C. Liu, M. Wang, J. Ye, L. Liu, L. Li, Y. Li and X. Huang, *Nano Lett.*, 2023, **23**, 1474–1480.

46 Q. Wang, M. Dai, H. Li, Y. R. Lu, T. S. Chan, C. Ma, K. Liu, J. Fu, W. Liao, S. Chen, E. Pensa, Y. Wang, S. Zhang, Y. Sun, E. Cortés and M. Liu, *Adv. Mater.*, 2023, **35**, 2300695.

47 X. Zhong, S. Liang, T. Yang, G. Zeng, Z. Zhong, H. Deng, L. Zhang and X. Sun, *ACS Nano*, 2022, **16**, 19210–19219.

48 J. A. Rebstock, Q. Zhu and L. R. Baker, *Chem. Sci.*, 2022, **13**, 7634–7643.

49 J. Hao, H. Zhu, Z. Zhuang, Q. Zhao, R. Yu, J. Hao, Q. Kang, S. Lu, X. Wang, J. Wu, D. Wang and M. Du, *ACS Nano*, 2023, **17**, 6955–6965.

50 S. Yang, M. Jiang, W. Zhang, Y. Hu, J. Liang, Y. Wang, Z. Tie and Z. Jin, *Adv. Funct. Mater.*, 2023, **33**, 2301984.

51 Y. Zhao, X.-G. Zhang, N. Bodappa, W.-M. Yang, Q. Liang, P. M. Radjenovica, Y.-H. Wang, Y.-J. Zhang, J.-C. Dong, Z.-Q. Tian and J.-F. Li, *Energy Environ. Sci.*, 2022, **15**, 3968–3977.

52 S. Yang, M. Jiang, W. Zhang, Y. Hu, J. Liang, Y. Wang, Z. Tie and Z. Jin, *Adv. Funct. Mater.*, 2023, **33**, 2301984.